Three-dimensional hollow nitrogen-doped carbon shells enclosed monodisperse CoP nanoparticles for long cycle-life sodium storage

Huang, Wei; Shangguan, Huihui; Zheng, Xiaowen; Engelbrekt, Christian; Yang, Yuan; Li, Shuo; Mølhave, Kristian; Xiao, Xinxin; Lin, Xiaohang; Ci, Lijie

Total number of authors:
11

Published in:
Electrochimica Acta

Link to article, DOI:
10.1016/j.electacta.2021.139112

Publication date:
2021

Document Version
Peer reviewed version

Three-dimensional hollow nitrogen-doped carbon shells enclosed monodisperse CoP nanoparticles for long cycle-life sodium storage

Wei Huang , Huihui Shangguan , Xiaowen Zheng , Christian Engelbrekt , Yuan Yang , Shuo Li , Kristian Mølhave , Xinxin Xiao , Xiaohang Lin , Lijie Ci , Pengchao Si

PII: S0013-4686(21)01402-X
DOI: https://doi.org/10.1016/j.electacta.2021.139112
Reference: EA 139112

To appear in: *Electrochimica Acta*

Received date: 31 May 2021
Accepted date: 13 August 2021

Please cite this article as: Wei Huang , Huihui Shangguan , Xiaowen Zheng , Christian Engelbrekt , Yuan Yang , Shuo Li , Kristian Mølhave , Xinxin Xiao , Xiaohang Lin , Lijie Ci , Pengchao Si , Three-dimensional hollow nitrogen-doped carbon shells enclosed monodisperse CoP nanoparticles for long cycle-life sodium storage, *Electrochimica Acta* (2021), doi: https://doi.org/10.1016/j.electacta.2021.139112

Three-dimensional hollow nitrogen-doped carbon shells enclosed monodisperse CoP nanoparticles for long cycle-life sodium storage

Wei Huang,[a, b] Huihui Shangguan,[a] Xiaowen Zheng, [a] Christian Engelbrekt, [b, c] Yuan Yang, [a] Shuo Li, [a] Kristian Mølhave, [d] Xinxin Xiao, [b] Xiaohang Lin,*[,a] Lijie Ci,[a] Pengchao Si,*[,a]

[a] *SDU & Rice Joint Center for Carbon Nanomaterials, Key Laboratory for Liquid-Solid Structural Evolution and Processing of Materials, Ministry of Education, School of Materials Science and Engineering, Shandong University, Jinan 250061, P. R. China.*

[b] *Department of Chemistry, Technical University of Denmark, DK-2800 Kongens Lyngby, Denmark.*

[c] *Department of Chemistry, University of California Irvine, Irvine, California, 92697, United States.*

[d] *DTU Nanolab-National Center for Nanofabrication and Characterization, Technical University of Denmark, DK-2800 Kongens Lyngby, Denmark.*

Corresponding Author: Dr. Xiaohang Lin, Shandong University, Key Laboratory for Liquid-Solid Structural Evolution and Processing of Materials, Ministry of Education, School of Materials Science and Engineering, Jinan 250061, China, E-mail: lxh12345@sdu.edu.cn, pcsi@sdu.edu.cn

Highlights

- Highly isolated CoP nanoparticles encapsulated in 3D hollow nitrogen-doped carbon shells.
- Unique porous 3D hollow architecture facilitates the transportation and storage of sodium ion.
- CoP/HNC delivers a long cycle-life capacity of 223 mA h g^{-1} after 700 cycles.
- Crucial factors related to the structural stability during cycling have been identified.

ABSTRACT: Transition metal phosphides are emerging as promising anode materials of

sodium ion batteries (SIBs) due to their high performance in terms of capacity and operational stability. Highly isolated CoP nanoparticles encapsulated in 3D hollow nitrogen-doped carbon networks (CoP/HNC composite) are designed via polymerization of poly-dopamine (PDA) on ZIF-67 and the subsequent in-situ phosphorization. Ultrafine CoP nanoparticles (10 ± 2 nm) are decorated in nitrogen-doped carbon polyhedral shells in a porous 3D hollow architecture. Benefiting from the unique construction, the CoP/HNC electrode delivers a high reversible long cycle-life capacity of 223 mA h g^{-1} for sodium storage at 500 mA g^{-1} after 700 cycles. DFT simulations indicate that Na atoms strongly bound to CoP surfaces, and significantly concentrate near CoP surfaces, beneficial for the Na atoms storage in this composite material. These results suggest the CoP/HNC composite can be a promising anode material for SIBs. Besides, the designed strategy of CoP/HNC composite could be applied to fabricate other metal phosphides for electrochemical storage devices.

Keywords: CoP; ZIF-67; PDA derived carbon; hollow structure; sodium storage.

1. Introduction

Developing durable and efficient energy storage systems for renewable energy holds the promise to alleviate the associated environmental issues of utilizing fossil fuels. Among multifarious electrochemical energy storage devices [1-3], sodium ion batteries (SIBs) are attracting considerable attention to replace lithium ion batteries (LIBs) due to the higher natural abundance of sodium [4-12]. However, the larger sodium ionic radius (1.02 Å) over that of the lithium (0.76 Å) results in sluggish ion diffusion kinetics and serious volume changes of active materials upon insertion and desertion, hindering the practical applications of SIBs and highlighting the importance of durable electrode materials [6, 13, 14].

Metal phosphides (e.g. FeP [15], SnP [16], CoP [17-19], Ni_2P [20, 21] etc.) are emerging for SIBs due to their high performance in terms of capacity and operational stability [15-21]. Two strategies are generally applied. The first strategy is the fabrication of nanostructured materials, which can effectively enhance reaction kinetics and reduce the steric hindrance

for sodium ions [15-17]. For example, Cabot and co-workers reported SnP nanocrystals based anode materials for SIBs with high reversible capacity of 600 mA h g^{-1} at 100 mA g^{-1} after 200 cycles [16]. However, Chou et al. synthesized nanosized CoP particles by a ball-milling strategy with a capacity of 315 mA h g^{-1} after only 25 cycles, without showing a long-term cycling ability [17]. The second strategy is the combination of metal phosphides with conductive carbonaceous networks, allowing to accommodate the significant volume change and enhance electrical conductivity [18-25]. Kang and co-workers used a conducting polymer coated CoP core–shell nanowires on the carbon paper as a free-standing anode for SIBs with a high areal capacity of 0.521 mA h cm^{-2} at 0.15 mA cm^{-2} after 100 cycles [18]. Xu et al. designed a sandwich-like Ni_2P nanoarray/nitrogen-doped graphene nanoarchitecture as SIBs anode with a high capacity of 188 mA h g^{-1} at 500 mA g^{-1} after 300 cycles [20]. Furthermore, hollow nanostructured carbonaceous matrices can be employed for good sodium ion storage [26-29]. For example, Yu et al. demonstrated hollow carbon sheet-encapsulated CuP_2 composites for SIBs with a high reversible specific capacity of 410 mA h g^{-1} at 80 mA g^{-1} after 200 cycles retaining 91% of the initial capacity. The good cycling performance was attributed to the preserved inner voids from the cross-linking carbon structure and nm-size of the particles [29]. In addition, introducing heteroatoms, especially nitrogen, into the carbonaceous materials could enhance the desired defect concentration for abundant active sites and the electrical conductivity for improved sodium ion storage [30-32]. For example, Maier and co-workers fabricated nitrogen doped porous carbon fibres as anode materials for sodium ion batteries with a good capacity of 243 mA h g^{-1} at 50 mA g^{-1} after 100 cycles [32]. While, only a few materials show the excellent capacity at high current density and long-term cycling performance for sodium ion storage [4]. To address the issue, synthesis of nanosized metal phosphides combined with nitrogen doped carbonaceous components all in one hollow material configuration could effectively increase the active sites, conductivity and capacitive capacity from the hollow carbonaceous materials, ensuring the good capacity and long-term cycling stability.

Metal-organic frameworks (MOFs) ,as a class of porous materials composed of metal sites and organic ligands, have been used as one of the most promising precursors to synthesize the nanomaterials with desired components and structure for electrochemical energy storage [33-38]. For example, Yin et al. synthesized metal-organic framework (MOF)-derived

CoP@C anchored on reduced graphene oxide (rGO) with a capacity of 473.1 mA h g^{-1} at 100 mA g^{-1} after 100 cycles (< 80% capacity retention). It is believed that the aggregated CoP nanoparticles limited the long-term cycle stability [37]. Li and co-workers reported ZIF-67 derived Co_2P@N-C@rGO with dual protection layers for sodium storage, with a capacity of 100 mA h g^{-1} at 1000 mA g^{-1} after 1000 cycles. The limited capacity may be due to the biggish CoP nanoparticles (120 nm) [38]. Inspired by these reports [37, 38], it appears that excellent cycling stability and capacity can be achieved by homogenously distributing cobalt phosphides with small particle sizes in MOFs derived carbonaceous networks for increased volume buffering ability and abundant active sites. This can be explained by the significant enhancement of the sodium ion diffusion and prevention of forming cracks in active materials due to volume change. To our best knowledge, there are few reports on controllable fabrication of designed integral hollow structure associated with homogenous cobalt phosphides and nitrogen-doped carbon shells for sodium ion storage.

Herein, highly isolated cobalt phosphide (CoP) nanoparticles encapsulated in three-dimensional hollow nitrogen-doped carbon shells (CoP/HNC) are constructed with initial polymerization of dopamine (PDA) on ZIF-67 and and the subsequent in-situ phosphorization. The obtained composites demonstrate an integral hollow architecture with highly uniform CoP nanoparticles (10 ± 2 nm) embedded in the nitrogen-doped carbon networks. When tested for the sodium ion storage, the CoP/HNC electrode delivers a high reversible long cycle-life capacity of 223 mA h g^{-1} at 500 mA g^{-1} after 700 cycles. The excellent sodium ion storage is attributed to combined effects of monodisperse CoP particles and nitrogen-doped carbon shells with hollow integral structure. DFT simulations further indicate that Na atoms strongly bound to CoP surfaces, and significantly concentrate near CoP surfaces, which are beneficial for the Na atoms storage in the composite.

2. Experimental section

2.1 Synthesis of Hollow CoP/HNC composite. ZIF-67 crystals were fabricated in a modified procedure which was previously reported [37]. Briefly, 498 mg $Co(NO_3)_2{\cdot}6H_2O$ (99%, Aladdin) and 656 mg 2-methylimidazole (98%, Aladdin) were dissolved in 100 mL methanol (≥ 99.5%, Sinopharm) to form an uniform solution, standing at room temperature for 24 h. After purifying with centrifugation and washing with methanol for at least three times, ZIF-

67 crystals were obtained. To form poly-dopamine (PDA) layers on the surfaces of ZIF-67 crystals [39], 50 mg dopamine hydrochloride (DAH, 98%, Aladdin) was dissolved in 50 mL Tris-HCl (10 mM, pH=8.5, Aladdin), into which 120 mg ZIF-67 crystals were added. The mixture was sonicated for 10 min and subsequently stirred for 24 h at room temperature. ZIF-67@PDA composites were obtained after washing with ultrapure water (>18.25 MΩ cm) and ethanol (≥ 99.7%, Sinopharm) more than three times and drying under vacuum. As-prepared ZIF-67@PDA composites were annealed at 550 °C for 1 h under nitrogen gas. The carbonized products were placed in a quartz boat, aligned with another boat containing NaH_2PO_2 (99%, Aladdin) with a mass ratio 3:1 to the carbonized products. Phosphorization was carried out at 350 °C for 2 h with the NaH_2PO_2 boat seating in the front of the Ar gas flow direction, leading to the final dark powder (CoP/HNC). As a control, CoP/NC composites were fabricated following the same protocol without PDA coating layers.

2.2 Materials characterization. Microstructures were analyzed by scanning electron microscopy (SEM, Quanta FEG 200 ESEM, 15 kV) and transmission electron microscopy (TEM, JEOL 2800, 200 kV; Tecnai G2 T20, 200 kV). Crystalline features of the composites were tested by X-ray diffraction (XRD, Miniflex 600, Cu-Kα radiation, λ = 1.5418 Å). Raman spectroscopy (Renishaw InVia Raman spectrometer, 633 nm Laser) and X-ray photoelectron spectroscopy (XPS, Thermo-Scientific system (Al-Kα radiation, 1484.6 eV) analysis were also conducted, respectively. Fourier transform infrared spectroscopy (FTIR, Vector 22 spectrometer, Bruker) was used to determine the surface functional groups. Specific surface area was estimated by a Surface Area & Pore Size Analyzer (ASAP 2020, Micromeritics). Thermal gravimetric analysis (TGA, Mettler-Toledo TGA/SDTA851e Thermo Analyzer) was conducted in air from room temperature to 750 °C with a heating rate of 5 °C min^{-1}.

2.3 Electrochemical measurements. Mixtures of the prepared materials (active materials, 70 wt%), super P (conductive agent, 20 wt%) and polyvinylidene fluoride (binder, PVDF, 10 wt%) were dissolved in N-methyl-2-pyrrolidone (NMP) and the slurry was casted onto a Cu foil to prepare working electrodes. Sodium foil was used as the counter and reference electrode. 1.0 M $NaClO_4$ dissolved in a mixed solvent (100: 5 vol%) consisting of propylene carbonate (PC) and fluoroethylene carbonate (FEC) was used as the electrolyte. Half coin cells (CR 2016) were assembled in a glove box under argon atmosphere at room temperature. Galvanostatic discharge/charge (GDC) testing in a voltage window of 0.01-3.0

V was recorded by a Neware-CT-3008 test system (Shenzhen, China). The calculated specific capacity is based on the mass of the whole CoP/HNC composite. Cyclic voltammograms (CVs) in the same voltage range at a scan rate of 0.1 mV s^{-1} were conducted at a CHI 660E electrochemical workstation (Shanghai, China). Electrochemical impedance spectroscopy (EIS) in a frequency range of 0.01 to 100 kHz was performed at the open circuit potential (OCP) by the Autolab instrument (Metrohm).

2.4 Computational details. The DFT calculations presented in this paper were performed using the periodic electronic structure code VASP [40], employing the Perdew, Burke and Ernzerhof (PBE) functional to describe the exchange and correlation effects[41]. The electron-core interactions were represented by the projected augmented wave method (PAW). The electronic one-particle wave functionals were expanded in a plane-wave basis setup to an energy cutoff of 600 eV. Different surfaces supercell sizes were employed in these studies, which had been make sure that the special k-points sets used to replace the integration over the first Brillouin zone are chosen large enough to get converged results. The structures were optimized by relaxing all adsorbed atoms and the uppermost several layers for CoP surfaces. The convergence of the results with respect to the parameters has been carefully checked.

The surface energy was defined as the surface excess free energy per unit area of a particular crystal face[42], which can be derived from an N-layer slab model for a unit area by:

$$\gamma = \frac{1}{2A}(E_{surf} - N * E_{bulk})$$

where E_{surf} is the total energy of the slab system, E_{bulk} is the bulk energy per atom, and A is the surface area of slab system.

The adsorption energy per Na atom was determined according to:

$$E_{ads} = (E_{tot} - E_{surf} - N * E_{Na})/N$$

where E_{tot} is the total energy of the system including substrate and adsorbate and E_{surf} and E_{Na} corresponds to the energy of a clean surface and a single Na atom respectively.

3. Results and discussion

The preparation process of ZIF-67@PDA and CoP/HNC composite has been investigated by monitoring their morphology evolution (Scheme 1). ZIF-67 crystals

(Fig. S1a and b) demonstrate a rhombic-dodecahedral shape, with a particle size of 1000 ± 200 nm (inset of Fig. S1a). As-prepared ZIF-67 crystals are soaked in the dopamine hydrochloride (DAH) solution to form PDA coating layers on the surface. During the polymerization process, the 2-methylimidazole (2-MIM) linkers of ZIF-67 become protonated in the Tris-HCl buffer solution (pH=8.5), leading to the breakdown of metal-ligand bonds and the decomposition of ZIF-67 crystals [43, 44]. Dopamine layers are simultaneously formed on the surfaces of the dissociating ZIF-67 crystals, with the free Co cations immobilized in the resulting PDA layers. Thus, the PDA layers maintain the skeleton of the polyhedral ZIF-67 crystals (Fig. S1c and d), labeled as hollow ZIF-67@PDA, which are confirmed by previous reports [39, 45]. After phosphorization, the Co cations and PDA layers in the ZIF-67@PDA are converted into CoP particles and nitrogen-doped carbon shells, respectively. The final product, i.e. CoP/HNC composite (Fig. 1a and b), preserves the initial polyhedral structure of ZIF-67 (1000 ± 200 nm) with an average size of 700 ± 100 nm. The decrease of particle size is mainly attributed to the decomposition of organic ligands in the composite during heating. In contrast, CoP embedded in the nitrogen-doped carbon (CoP/NC) without PDA coating layers (Fig. S2) shows a constringent polyhedral morphology after annealing.

Transmission electron microscopy (TEM) characterization of the ZIF-67@PDA (Fig. S3) and CoP/HNC (Fig. 1c and d) was performed. ZIF-67@PDA shows an obviously hollow polyhedral morphology. After phosphorization, CoP/HNC (Fig. 1c and d) displays highly dispersed cobalt phosphide nanoparticles, which are uniformly locked in the 3D hollow nitrogen-doped carbon shells. The average particle size of CoP nanoparticles (Fig. 1e) is 10 ± 2 nm. TEM images of the edge (Fig. 1f) and interior (Fig. 1g) of a single CoP/HNC particle further suggest the homogenous distribution of CoP nanoparticles and abundant interspace between CoP nanoparticles and carbon shells. Numerous nanovoids (Fig. 1d, f and g) on the hollow carbon polyhedron are clearly observed, originating from the decomposition of organic groups during solid/gas-phase phosphorization. As a control, CoP/NC (Fig. S4) shows that CoP nanoparticles homogenously disperse in the carbon networks without hollow inner voids. Moreover, the high-resolution TEM image of CoP/HNC (Fig. 1h) clearly reveals the CoP nanoparticles are embedded in amorphous carbon shells. The lattice fringe in Fig. 2h is calculated to be 0.247 nm, assigned to the (111) lattice plane of CoP [18]. Scanning-TEM

and EDS mapping (STEM-EDS) images of a polyhedron (Fig. S5) further verify the uniform elemental distribution of the material. STEM-EDS results of single CoP/HNC polyhedron clearly show the homogenous distribution of C, N, O, Co and P (Fig. 1i-m). The elemental oxygen is mainly from the carbon shells derived from the PDA layers and partial oxidation of CoP. The hollow skeleton of uniform cobalt and phosphorus elements encapsulated in nitrogen-doped carbon frameworks are further confirmed by bright-field (Fig. 1n), dark-field (Fig. 1o), superimposed EDS elemental map (Fig. 1p-r) and secondary electron (Fig. 1s) images. This is further highlighted in a line plot across a single CoP/HNC particle (Fig. S6), the contents of Co, P, O, N and C elements are clearly shown in the single polyhedral structure, the stable nitrogen content indicates the uniform nitrogen doping in the carbon shells. It is noteworthy that the contents of cobalt and phosphorus elements are nearly same, implying the successful preparation of CoP.

The crystalline features of CoP/HNC (Fig. 2a) were further characterized by X-ray diffraction (XRD). The obvious diffraction peaks match well with planes of CoP (JCPDS no. 89-4862). In addition, the Raman spectrum of CoP/HNC (Fig. 2b) suggests the existence of amorphous carbon with D band at 1338 cm^{-1} and G band at 1581 cm^{-1}. Due to the D band is related to the disordered graphite from disorders or defects of structures, and the G band is assigned to the vibration of the sp^2 hybridized carbon bonding. Higher intensity of G band than D band indicates the high graphitization degree of CoP/HNC composite. In contrast, the Raman spectrum of CoP/NC (Fig. 2b) possesses near same intensities of D band and G band. These results suggest that the introduction of PDA derived carbon layers in the CoP/HNC composite efficiently improve the electrical conductivity [35, 46]. In addition, surface functional groups of synthetic materials are characterized by Fourier transform infrared spectroscopy (FTIR, Fig. S7). In the spectrum of ZIF-67, the peaks in the range from 600 to 1500 cm^{-1} are assigned to the stretching and bending of the imidazole group [47]. The peak at 427 cm^{-1} is ascribed to Co-N stretching vibrations of ZIF-67 [39]. After incorporating the PDA layers on the surface of ZIF-67, the corresponded bands of ZIF-67 become weak in the ZIF-67@PDA, indicating the dissociation of ZIF-67 crystals. Besides, the band in the range of 1450–1670 cm^{-1} is attributed to the C-C vibration of the benzene ring in the dopamine molecules [48]. Furthermore, The FTIR of CoP/HNC composite exhibits C-O vibration (1100 cm^{-1}) and Co-O stretching vibrations (558 cm^{-1}), respectively. The observation suggests that the organic groups transform to the inorganic carbon components and the partial

oxidization of the surface CoP after phosphorization. The broad bands at 3200–3400 cm^{-1} is belonged to the O-H vibrations. The chemical states of the CoP/HNC composite are analyzed by X-ray photoelectron spectroscopy (XPS). The survey spectrum (Fig. S8) suggests the presences of Co, P, N and C. In the high-resolution Co 2p spectrum (Fig. S9a), doublets with Co $2p_{3/2}$ components at 778.8 and 781.8 eV are assigned to the Co-P bond and oxidized Co species on the surface of CoP, respectively. Two peaks at 786.2 and 803.4 eV correspond to the accompanying satellite signals [49, 50]. The P 2p spectrum (Fig. S9b) is fitted into two doublets with a 0.9 eV separation associating with phosphide (129.7 eV) and oxidized P (133.6 eV) [49-51]. The N 1s spectrum (Fig. S9c) can be divided into five peaks corresponding to the pyridinic-N (398.5 eV), amino-N (399.5 eV), pyrrolic-N (400.3 eV), graphitic-N (401.3 eV) and oxidized-N (403.3 eV), indicative of successful preparation of nitrogen-doped carbon [52, 53]. The C 1s spectrum (Fig. S9d) presents characteristic peaks assigned to sp^2 C-C (284.6 eV), sp^3 C-C (285.4 eV), C-N (285.9 eV), C-O (286.9 eV) and C=O (289.1 eV) bonds [54, 55].

The components of CoP/HNC were investigated by thermal gravimetric analysis (TGA, Fig. S10) in air from room temperature to 750 °C. The initial weight loss (< 150 °C) is assigned to the volatilization of gaseous component and H_2O. The following weight increase (150-255 °C) is due to the partial oxidation of cobalt phosphides. A drastic weight loss (255-400 °C) is ascribed to the combustion of carbonaceous ingredients in the composites. A gradual weight increase is observed in the range of 400-600 °C, attributed to the further oxidation of cobalt phosphide [36]. The weight almost maintained constant when temperature is above 650 °C. A total weight loss of 34.5 % corresponded the weight ratio of CoP content in the composite to be 73.4 %. Moreover, the Brunauer-Emmett-Teller (BET) surface area of the CoP/HNC composite is measured to be 202.6 $m^2 g^{-1}$ (Fig. 3a), almost 10-fold of that of the constricted CoP/NC composite (21.1 $m^2 g^{-1}$). The larger specific surface area for CoP/HNC is mainly attributed to the hollow inner voids and pore-forming effects from the generation of gaseous components in the composite [8], which is confirmed by the TEM results (Fig. 1c, d, f and g). The pore-size distribution of CoP/HNC (Fig. 3b) indicates that most pores are in the mesoporous range (2-15 nm), which are from the interspace between CoP nanoparticles and carbon shells. Micropores and macropores originate from the PDA derived carbon and the hollow interior structure. The hierarchical pores are believed to be beneficial to sodium-ion diffusion and storage.

The sodium ion storage performance of the CoP/HNC composite was tested in a half-cell configuration. Fig. 4a shows the cyclic voltammograms (CVs) of the initial four cycles at 0.1 mV s^{-1}. In the first cathodic scan, two sharp reduction peaks at 0.85 and 0.55 V correspond to the irreversible generation of solid electrolyte interface (SEI) film, the formation of Na_3P and Co and the insertion of sodium ion into the nitrogen-doped carbon shells [18, 56, 57]. Two broad oxidation peaks in the first anodic scan at 0.35 and 1.30 V are ascribed to the sodium ion extraction from nitrogen-doped carbon shells and the desodiation of Na_3P [18, 57, 58]. The subsequent cycles see the cathodic peaks shift to 0.40 and 1.2 V, and the anodic peaks to 0.20 and 1.35 V. The shift phenomena may be stemmed from the contact resistance between copper foil substrate and active materials [59]. In order to further analyze the electrochemical reaction of CoP/HNC for sodium ion storage, the CVs (Fig. S11a) at 0.1 mV s^{-1} of bare carbon (90 wt% super P and 10 wt% PVDF) assembled half-coin cells were investigated. The bare carbon demonstrates a couple of redox peaks at 0.45 and 0.15 V from the second cycle on, matching well with the corresponded peaks in the CVs of CoP/HNC. Thus, the sodium ion storage process of CoP/HNC is mainly attributed to the combined effects from the alloying reaction of sodium ion with phosphorus from the initial cobalt phosphorus and intercalation reaction of nitrogen-doped carbon with sodium ion.

The galvanostatic discharge/charge profiles of the initial four cycles at 100 mA g^{-1} for CoP/HNC are shown in Fig. 4b. The first discharge voltage plateau in the range of 1.2 - 0.4 V matches well with reductive peaks of the initial cycle of CVs (Fig. 4a), a slow slope is observed during the first charge process (Fig. 4b), corresponding to the oxidative reaction of the first cycle of CVs (Fig. 4a). In addition, the profiles (Fig. 4b) overlap well after the first cycle, indicating a well reversible process. Fig. 4c shows the cycling performance of CoP/HNC at 100 mA g^{-1}. The initial discharge and charge capacities of CoP/HNC are calculated to be 701 and 353 mA h g^{-1}, respectively, with a relatively low Coulombic efficiency of 50.4%. This irreversible capacity loss is due to the formation of SEI film and partial decomposition of electrolyte in the first cycle. The Coulombic efficiency is over 96% since the 3th cycle. CoP/HNC delivers a discharge capacity of 304 mA h g^{-1} after 100 cycles, showing a good cycling stability, in contrast to 197 mA h g^{-1} after 100 cycles for CoP/NC (Fig. S12a). The better cycling performance of CoP/HNC is mainly attributed to the presence of the hollow inner structure, exhibiting larger surface area and more active sites. The rate capability at different current densities (100, 200, 500, 1000 and 2000 mA g^{-1}) of CoP/HNC is shown in Fig.

4d. CoP/HNC retains discharge capacities of 339, 271, 215, 175 and 133 mA h g^{-1}, respectively. When the current density is returned to 100 mA g^{-1}, the discharge capacity of CoP/HNC recovers to 318 mA h g^{-1}. As a control, the discharge capacities (Fig. S12b) of CoP/NC are 128, 115, 101, 89, 75 and 127 mA h g^{-1} at the current densities of 100, 200, 500, 1000, 2000 and 100 mA g^{-1}, respectively. The remarkable rate performance of CoP/HNC is attributed to unique microstructure of the nitrogen-doped hollow carbon shells displaying ultrafine monodisperse CoP nanoparticles, which is believed to effectively buffer the volume expansion during the high-rate discharge/charge processes.

The long-term cycling performance of CoP/HNC at a high current density of 500 mA g^{-1} is shown in Fig. 4e. The initial discharge and charge capacities of CoP/HNC are 589 and 273 mA h g^{-1}, respectively. After activation over five cycles, a stable discharge capacity of 233 mA h g^{-1} is achieved. CoP/HNC still delivers a discharge capacity of 223 mA h g^{-1} after 700 cycles, with a capacity retention of 95.7% compared with the 6th cycle. The Coulombic efficiency is more than 95 % after the initial three cycles. In comparison, CoP/NC (Fig. S13) demonstrates an initial discharge and charge capacities of 354 and 151 mA h g^{-1}, respectively, and a discharge capacity of 168 mA h g^{-1} after 700 cycles. Besides, the first discharge/ charge capacities of bare carbon (Fig. S11b) are 233/49 mA h g^{-1}, the bare carbon only exhibits a discharge capacity of 58 mA h g^{-1} after 200 cycles. Thus, the good long-term cycling performance of CoP/HNC is mainly attributed to the combined effects from the monodisperse CoP nanoparticles and hollow nitrogen-doped carbon shells for sodium ion storage, and the hollow framework could efficiently accommodate the volume changes during cycling at high current density. In addition, it's safe to conclude that, in contrast with CoP/NC and many previously reported metal phosphides related systems for sodium storage (Table S1), CoP/HNC shows an excellent long cycle-life sodium storage.

To better understand the merits of the CoP/HNC composite, electrochemical impedance spectroscopy (EIS) is performed (Fig. S14). The middle frequency region on the Nyquist plot corresponds to charge transfer resistance of sodium ions [10]. The charge transfer resistance for CoP/HNC (R_{ct} = 40 Ω) is lower than that of CoP/NC (R_{ct} = 253 Ω) before cycling, suggesting an enhanced electrical conductivity of CoP/HNC with the PDA derived carbon modification. SEM and TEM images (Fig. S15)

of CoP/HNC electrode materials after 100 cycles at 100 mA g^{-1} further indicate nanoparticles are firmly enclosed in hollow nitrogen-doped carbon shells, confirming the structural stability of CoP/HNC composite during discharge-charge cycling. The excellent electrochemical performance of CoP/HNC for sodium ion storage, especially the long-term cycling stability and superior rate capability are mainly due to the synergistic effects from the unique porous hollow configuration with highly isolated CoP nanoparticles and porous carbon shells. As illustrated in Fig. 4f, uniform CoP nanoparticles (10 ± 2 nm) can effectively shorten the sodium ion diffusion lengths for high-rate performance. In addition, highly conductive carbon shells promote electronic conductivity of the composite, leading to fast charge transfer for sodium ion storage during the discharge/charge process. Besides, nitrogen doping in the carbon shells not only increases the electronic conductivity of electrode material, but also provides abundant defects acting as active sites for the sodium-ion insertion/extraction [9, 53]. Moreover, the internal hollow structure and nanopores in the carbon matrix facilitates a continuous and effective electron transfer, and sodium ion transport and storage for long cycle-life stability.

To illustrate the experimental results more forcefully, the DFT simulations were also performed. The structure of CoP crystal is orthorhombic within the space group Pnma. There are four Co and P atoms in one unit cell (Fig. S16). The magnetic properties including paramagnetic, ferromagnetic and several kinds of antiferromagnetic structures have been considered. The most stable structure is the paramagnetic structure, which agrees with experimental result. The lattice parameters are calculated to be a=5.068Å, b=3.267 Å and c=5.550 Å, which only differs by 0.1% from the experimental data[60].

To analysis and explain the phenomenon preliminarily, the adsorption trend of Na atom on observed CoP surfaces are investigated. Note that, only the surfaces observed in the XRD results (CoP(111), CoP(110) and CoP(211) surface) are calculated. For the complex compounds like CoP, there are several different surfaces in every family of crystal planes. As the first step, we determined the most stable surface structure of every family of crystal planes (Fig. S17). Every surface has rather open and complicated structure. After relaxation, the outermost layer distance contracts a little bit, but no surface reconstruction is found. These trends can be explained in terms of the correlation between bond strength and

coordination[61]. The unitcell was shown in the top view of each surface. All possible adsorption positions for Na atom are also marked in the top view of Fig. S17.

Then we determined the optimum adsorption position of a Na adatom on CoP surfaces (see Fig. 5). For CoP(111) we find that the equilibrium position is the threefold hollow site of Phosphorus atoms (Fig. 3a). the average distance to the nearest neighboring P atoms is 0.28 nm. For CoP(110) and CoP(211) surfaces, the results are quite similar, the adatom prefers to adsorb at a “shallow pits” of the surfaces. The average distance to the nearest neighboring P atoms are 0.31 nm and 0.30 nm, respectively. Although the Na-P bond length on CoP(211) is 0.03 nm larger than on CoP(111) surface, the adsorption energy is even 0.3 eV larger (Table 1). This can be explained by the fact that the coordinate number of the Na atom (5 atoms) on CoP(211) is much larger than on CoP(111) surface (3 atoms). At CoP surfaces, we find similar adsorption energy of about -2 eV, which is about 4 times larger than on graphite (0001) surface (Table 1). Such large adsorption energy indicates that Na atoms strongly bound to CoP surfaces, and significantly concentrate near CoP surfaces.

In order to obtain a deeper understanding of the properties of Na atom on CoP surfaces, we have also analyzed their electronic structures. There is a significant charge transfer between Na atom and CoP surfaces. This is illustrated in Fig. 6a, b, c where isosurfaces of the charge density differences upon Na atom adsorption on CoP(111), CoP(110) and CoP(211) are plotted. The charge rearrangement is mainly localized near the adsorption position. There is a particular strong charge accumulation of electron density near the surface below the Na atom whereas there is considerable charge depletion around Na atom (Fig. 6a, b and c). This suggests a strong interaction between the adatom and surfaces, which prove the results of adsorption energy from another point of view. The charge depletion around Na atom indicates an ionic bond between Na and P atoms. The LDOS (Fig. 6d) and Bader analysis also gives the same result. There are only 10.06 electrons around Na atoms, which mean one electron transfer from Na-3s orbital to the surface. Obviously, the strong attractive interactions between Na atom and CoP surfaces will lead to a concentration of Na ions near electrode. Note that, the adsorption energy on different CoP surfaces do not differ substantially will lead to a homogeneous distribution of Na ions near CoP interfaces. In our opinion, this is the main reason that our material has so high charging speed and large capacity. The simulation results accord well with the experimental results, illustrating again the excellent energy storage performance of the CoP/HNC composite.

4. Conclusion

In summary, the CoP/HNC composite is successfully synthesized and applied for the anode materials of SIBs. CoP particles (10 ± 2 nm) are homogenously dispersed in the 3D nitrogen-doped carbon polyhedral skeletons with an integral hollow configuration. This structural design not only effectively enhances the electronic and ionic conductivity of the composite for improved sodium-ion storage, but also efficiently accommodates the volume change for good cycling stability. Therefore, the composite delivers a high capacity of 304 mA h g^{-1} at 100 mA g^{-1} after 100 cycles, with a superior long cycle-life capacity of 223 mA h g^{-1} at 500 mA g^{-1} after 700 cycles. DFT simulations demonstrate that Na atoms strongly bound to CoP surfaces, and are significantly concentrated near CoP surfaces, which are beneficial for the Na atoms storage in this composite material. These results confirm the CoP/HNC composite could be used as a promising anode material for SIBs. Besides, the designed strategy of CoP/HNC composite could be applied to fabricate other metal phosphides for electrochemical storage and conversion technologies.

mmc1.docx

Declaration of Competing Interest

The authors declare that they have no known competing financial interests or personal relationships that could have appeared to influence the work reported in this paper.

Associated content

Supporting information.

The Supporting Information is available free of charge.

The supporting figures including XPS patterns, TEM images, EDS spectra and mapping images, structure of CoP unit cell, minimum-energy surface structures, and electrochemical data with those reported in literatures.

Notes

The authors declare no competing financial interest.

Acknowledgements

The work is supported by Shandong Provincial Science and Technology Major (2018JMRH0211, 2016GGX104001, 2017CXGC1010 and ZR2017MEM002), the Fundamental Research Funds of Shandong University (2016JC005, 2017JC042 and 2017JC010) and 1000 Talent Plan program (No. 31370086963030), Chinese Scholarship Council (201706220080), Danish Council for Independent Research (DFT-1335-00330), Villum Experiment (grant No. 35844), Independent Research Fund Denmark (DFF-5054-00107). TEM work was partly performed at the UC Irvine Materials Research Institute (IMRI).

References

[1] J.-M. Tarascon, M. Armand, Issues and challenges facing rechargeable lithium batteries, Nature, 414 (2001) 359-367.
[2] M. Li, J. Lu, X. Ji, Y. Li, Y. Shao, Z. Chen, C. Zhong, K. Amine, Design strategies for nonaqueous multivalent-ion and monovalent-ion battery anodes, Nat. Rev. Mater., 5 (2020) 276-294.
[3] L. Zhang, W. Wang, S. Lu, Y. Xiang, Carbon Anode Materials: A Detailed Comparison between Na-ion and K-ion Batteries, Adv. Energy Mater., (2021) 2003640.
[4] N. Yabuuchi, K. Kubota, M. Dahbi, S. Komaba, Research development on sodium-ion batteries, Chem. Rev., 114 (2014) 11636-11682.
[5] X. Wei, X. Wang, X. Tan, Q. An, L. Mai, Nanostructured conversion-type negative electrode materials for low-cost and high-performance sodium-ion batteries, Adv. Funct. Mater., 28 (2018) 1804458.
[6] P.K. Nayak, L. Yang, W. Brehm, P. Adelhelm, From lithium-ion to sodium-ion batteries: advantages, challenges, and surprises, Angew. Chem. Int. Ed., 57 (2018) 102-120.
[7] X. Dou, I. Hasa, D. Saurel, C. Vaalma, L. Wu, D. Buchholz, D. Bresser, S. Komaba, S. Passerini, Hard carbons for sodium-ion batteries: Structure, analysis, sustainability, and electrochemistry, Mater. Today, 23 (2019) 87-104.
[8] J.S. Cho, J.-S. Park, Y.C. Kang, Porous FeS nanofibers with numerous nanovoids obtained by Kirkendall diffusion effect for use as anode materials for sodium-ion batteries, Nano Res., 10 (2017) 897-907.

[9] F. Zhang, E. Alhajji, Y. Lei, N. Kurra, H.N. Alshareef, Highly doped 3D graphene Na-ion battery anode by laser scribing polyimide films in nitrogen ambient, Adv. Energy Mater., 8 (2018) 1800353.
[10] W. Huang, H. Sun, H. Shangguan, X. Cao, X. Xiao, F. Shen, K. Mølhave, L. Ci, P. Si, J. Zhang, Three-dimensional iron sulfide-carbon interlocked graphene composites for high-performance sodium-ion storage, Nanoscale, 10 (2018) 7851-7859.
[11] Y. Wang, P. Niu, J. Li, S. Wang, L. Li, Recent progress of phosphorus composite anodes for sodium/potassium ion batteries, Energy Storage Mater., 34 (2021) 436-460.
[12] P. Cai, K. Zou, X. Deng, B. Wang, M. Zheng, L. Li, H. Hou, G. Zou, X. Ji, Comprehensive understanding of sodium-ion capacitors: Definition, mechanisms, configurations, materials, key technologies, and future developments, Adv. Energy Mater., 11 (2021) 2003804.
[13] G.-L. Xu, R. Amine, A. Abouimrane, H. Che, M. Dahbi, Z.-F. Ma, I. Saadoune, J. Alami, W.L. Mattis, F. Pan, Challenges in developing electrodes, electrolytes, and diagnostics tools to understand and advance sodium-ion batteries, Adv. Energy Mater., 8 (2018) 1702403.
[14] H. Shuai, J. Li, F. Jiang, X. Zhang, L. Xu, J. Hu, H. Hou, G. Zou, W. Sun, H. Duan, J. Hu, X. Ji, Electrochemically intercalated intermediate induced exfoliation of few-layer MoS_2 from molybdenite for long-life sodium storage, Sci. China Mater., 64 (2021) 115-127.
[15] Y. Wang, C. Wu, Z. Wu, G. Cui, F. Xie, X. Guo, X. Sun, FeP nanorod arrays on carbon cloth: a high-performance anode for sodium-ion batteries, Chem. Commun., 54 (2018) 9341-9344.
[16] J. Liu, S. Wang, K. Kravchyk, M. Ibáñez, F. Krumeich, R. Widmer, D. Nasiou, M. Meyns, J. Llorca, J. Arbiol, SnP nanocrystals as anode materials for Na-ion batteries, J. Mater. Chem. A, 6 (2018) 10958-10966.
[17] W.-J. Li, Q.-R. Yang, S.-L. Chou, J.-Z. Wang, H.-K. Liu, Cobalt phosphide as a new anode material for sodium storage, J. Power Sources, 294 (2015) 627-632.
[18] J. Zhang, K. Zhang, J. Yang, G.-H. Lee, J. Shin, V. Wing-hei Lau, Y.-M. Kang, Bifunctional conducting polymer coated CoP core-shell nanowires on carbon paper as a free-standing anode for sodium ion batteries, Adv. Energy Mater., 8 (2018) 1800283.
[19] K. Zhang, M. Park, J. Zhang, G.-H. Lee, J. Shin, Y.-M. Kang, Cobalt phosphide nanoparticles embedded in nitrogen-doped carbon nanosheets: Promising anode material with high rate capability and long cycle life for sodium-ion batteries, Nano Res., 10 (2017) 4337-4350.
[20] C. Dong, L. Guo, Y. He, C. Chen, Y. Qian, Y. Chen, L. Xu, Sandwich-like Ni_2P nanoarray/nitrogen-doped graphene nanoarchitecture as a high-performance anode for sodium and lithium ion batteries, Energy Storage Mater., 15 (2018) 234-241.
[21] C. Wu, P. Kopold, P.A. van Aken, J. Maier, Y. Yu, High performance graphene/Ni_2P hybrid anodes for lithium and sodium storage through 3D yolk-shell-like nanostructural design, Adva. Mater., 29 (2017) 1604015.
[22] Z. Yang, Q. Pan, Z. Wu, W. Xiang, F. Fu, Y. Wang, L. Ji, B. Zhong, X. Sun, X. Guo, Self-supported cobalt phosphate nanoarray with pseudocapacitive behavior: An efficient 3D anode material for sodium-ion batteries, J. Alloys Compd., 848 (2020) 156285.
[23] Q. Chang, Y. Jin, M. Jia, Q. Yuan, C. Zhao, M. Jia, Sulfur-doped CoP@ nitrogen-doped porous carbon hollow tube as an advanced anode with excellent cycling stability for sodium-ion batteries, J. Colloid Interface Sci., 575 (2020) 61-68.
[24] Q. Liu, Z. Hu, Y. Liang, L. Li, C. Zou, H. Jin, S. Wang, H. Lu, Q. Gu, S.-L. Chou, Y. Liu, S.-X. Dou, Facile Synthesis of Hierarchical Hollow CoP@C Composites with Superior Performance for Sodium and Potassium Storage, Angew. Chem. Int. Ed., 59 (2020) 5159-5164.
[25] H. Su, Y. Zhang, X. Liu, F. Fu, J. Ma, K. Li, W. Zhang, J. Zhang, D. Li, Construction of CoP@C embedded into N/S-co-doped porous carbon sheets for superior lithium and sodium storage, J. Colloid Interface Sci., 582 (2021) 969-976.
[26] J. Nai, X.W.D. Lou, Hollow structures based on prussian blue and its analogs for electrochemical energy storage and conversion, Adv. Mater., (2018) 1706825.
[27] F. Xie, L. Zhang, C. Ye, M. Jaroniec, S.-Z. Qiao, The application of hollow structured anodes for sodium-ion batteries: from simple to complex systems, Adv. Mater., (2018) 1800492.

[28] Y. Fang, X.-Y. Yu, X.W.D. Lou, Bullet-like Cu_9S_5 hollow particles coated with nitrogen-doped carbon for sodium-ion batteries, Angew. Chem. Int. Ed., 58 (2019) 7744-7748.
[29] S. Chen, F. Wu, L. Shen, Y. Huang, S.K. Sinha, V. Srot, P.A. van Aken, J. Maier, Y. Yu, Cross-linking hollow carbon sheet encapsulated CuP_2 nanocomposites for high energy density sodium-ion batteries, ACS Nano, 12 (2018) 7018-7027.
[30] W. Shen, C. Wang, Q. Xu, H. Liu, Y. Wang, Nitrogen-doping-induced defects of a carbon coating layer facilitate Na-storage in electrode materials, Adv. Energy Mater., 5 (2015) 1400982.
[31] Y. Zhao, F. Wang, C. Wang, S. Wang, C. Wang, Z. Zhao, L. Duan, Y. Liu, Y. Wu, W. Li, D. Zhao, Encapsulating highly crystallized mesoporous Fe_3O_4 in hollow N-doped carbon nanospheres for high-capacity long-life sodium-ion batteries, Nano Energy, 56 (2019) 426-433.
[32] L. Fu, K. Tang, K. Song, P.A. van Aken, Y. Yu, J. Maier, Nitrogen doped porous carbon fibres as anode materials for sodium ion batteries with excellent rate performance, Nanoscale, 6 (2014) 1384-1389.
[33] C. Wang, Y.V. Kaneti, Y. Bando, J. Lin, C. Liu, J. Li, Y. Yamauchi, Metal-organic framework-derived one-dimensional porous or hollow carbon-based nanofibers for energy storage and conversion, Mater. Horiz., 5 (2018) 394-407.
[34] G. Zou, H. Hou, P. Ge, Z. Huang, G. Zhao, D. Yin, X. Ji, Metal-organic framework-derived materials for sodium energy storage, Small, 14 (2018) 1702648.
[35] W. Huang, S. Li, X. Cao, C. Hou, Z. Zhang, J. Feng, L. Ci, P. Si, Q. Chi, Metal-organic framework derived iron sulfide-carbon core-shell nanorods as a conversion-type battery material, ACS Sustainable Chem. Eng., 5 (2017) 5039-5048.
[36] G. Xia, J. Su, M. Li, P. Jiang, Y. Yang, Q. Chen, A MOF-derived self-template strategy toward cobalt phosphide electrodes with ultralong cycle life and high capacity, J. Mater. Chem. A, 5 (2017) 10321-10327.
[37] X. Ge, Z. Li, L. Yin, Metal-organic frameworks derived porous core/shellCoP@ C polyhedrons anchored on 3D reduced graphene oxide networks as anode for sodium-ion battery, Nano Energy, 32 (2017) 117-124.
[38] R. Jin, X. Li, Y. Sun, H. Shan, L. Fan, D. Li, X. Sun, Metal–organic frameworks-derived Co_2P@ NC@ rGO with dual protection layers for improved sodium storage, ACS Appl. Mater. interfaces, 10 (2018) 14641-14648.
[39] H. Shangguan, W. Huang, C. Engelbrekt, X. Zheng, F. Shen, X. Xiao, L. Ci, P. Si, J. Zhang, Well-defined cobalt sulfide nanoparticles locked in 3D hollow nitrogen-doped carbon shells for superior lithium and sodium storage, Energy Storage Mater., 18 (2019) 114-124.
[40] G. Kresse, J. Furthmüller, Efficient iterative schemes for ab initio total-energy calculations using a plane-wave basis set, Physical review B, 54 (1996) 11169-11186.
[41] J.P. Perdew, K. Burke, M. Ernzerhof, Generalized gradient approximation made simple, Physical review letters, 77 (1996) 3865.
[42] A. Groß, Theoretical surface science, A Microscopic Perspective. Originally published in the series: Advanced Texts in Physics, 132 (2003).
[43] H. Zhang, D. Liu, Y. Yao, B. Zhang, Y.S. Lin, Stability of ZIF-8 membranes and crystalline powders in water at room temperature, J.Membr. Sci., 485 (2015) 103-111.
[44] C. Avci, J. Ariñez-Soriano, A. Carné-Sánchez, V. Guillerm, C. Carbonell, I. Imaz, D. Maspoch, Post-synthetic anisotropic wet-chemical etching of colloidal sodalite ZIF crystals, Angew. Chem. Int. Ed, 54 (2015) 14417-14421.
[45] Y. Yang, S. Li, W. Huang, H. Shangguan, C. Engelbrekt, S. Duan, L. Ci, P. Si, Effective synthetic strategy for $Zn_{0.76}Co_{0.24}S$ encapsulated in stabilized N-doped carbon nanoarchitecture towards ultra-long-life hybrid supercapacitors, J. Mater. Chem. A, 7 (2019) 14670-14680.
[46] H. Shuai, P. Ge, W. Hong, S. Li, J. Hu, H. Hou, G. Zou, X. Ji, Electrochemically exfoliated phosphorene–graphene hybrid for sodium-ion batteries, Small Methods, 3 (2019) 1800328.

[47] H.T. Kwon, H.-K. Jeong, A.S. Lee, H.S. An, J.S. Lee, Heteroepitaxially grown zeolitic imidazolate framework membranes with unprecedented propylene/propane separation performances, J. Am. Chem. Soc., 137 (2015) 12304-12311.
[48] Z. Ghelichkhah, S. Sharifi-Asl, K. Farhadi, S. Banisaied, S. Ahmadi, D.D. Macdonald, L-cysteine/polydopamine nanoparticle-coatings for copper corrosion protection, Corros. Sci., 91 (2015) 129-139.
[49] Y.-P. Zhu, Y.-P. Liu, T.-Z. Ren, Z.-Y. Yuan, Self-supported cobalt phosphide mesoporous nanorod arrays: a flexible and bifunctional electrode for highly active electrocatalytic water reduction and oxidation, Adv. Funct. Mater., 25 (2015) 7337-7347.
[50] Y. Hou, Y. Liu, R. Gao, Q. Li, H. Guo, A. Goswami, R. Zboril, M.B. Gawande, X. Zou, Ag@ Co_xP core-shell heterogeneous nanoparticles as efficient oxygen evolution reaction catalysts, ACS Catal., 7 (2017) 7038-7042.
[51] R. Wu, D.P. Wang, K. Zhou, N. Srikanth, J. Wei, Z. Chen, Porous cobalt phosphide/graphitic carbon polyhedral hybrid composites for efficient oxygen evolution reactions, J. Mater. Chem. A, 4 (2016) 13742-13745.
[52] J.R. Pels, F. Kapteijn, J.A. Moulijn, Q. Zhu, K.M. Thomas, Evolution of nitrogen functionalities in carbonaceous materials during pyrolysis, Carbon, 33 (1995) 1641-1653.
[53] D. Zhou, Y. Cui, P.-W. Xiao, M.-Y. Jiang, B.-H. Han, A general and scalable synthesis approach to porous graphene, Nat. Commun., 5 (2014) 4716.
[54] X. Yang, J. Li, J. Liu, Y. Tian, B. Li, K. Cao, S. Liu, M. Hou, S. Li, L. Ma, Simple small molecule carbon source strategy for synthesis of functional hydrothermal carbon: preparation of highly efficient uranium selective solid phase extractant, J. Mater. Chem. A, 2 (2014) 1550-1559.
[55] R.R. Salunkhe, J. Tang, Y. Kamachi, T. Nakato, J.H. Kim, Y. Yamauchi, Asymmetric supercapacitors using 3D nanoporous carbon and cobalt oxide electrodes synthesized from a single metal-organic framework, ACS Nano, 9 (2015) 6288-6296.
[56] W.-J. Li, S.-L. Chou, J.-Z. Wang, H.-K. Liu, S.-X. Dou, Simply mixed commercial red phosphorus and carbon nanotube composite with exceptionally reversible sodium-ion storage, Nano lett., 13 (2013) 5480-5484.
[57] F. Xie, Z. Xu, A.C.S. Jensen, H. Au, Y. Lu, V. Araullo-Peters, A.J. Drew, Y.-S. Hu, M.-M. Titirici, Hard–soft carbon composite anodes with synergistic sodium storage performance, Adv. Funct. Mater., 29 (2019) 1901072.
[58] J. Qian, X. Wu, Y. Cao, X. Ai, H. Yang, High capacity and rate capability of amorphous phosphorus for sodium ion batteries, Angew. Chem. Int. Ed., 52 (2013) 4633-4636.
[59] T. Jiang, S. Zhang, X. Qiu, W. Zhu, L. Chen, Preparation and characterization of silicon-based three-dimensional cellular anode for lithium ion battery, Electrochem. Commun., 9 (2007) 930-934.
[60] K. Selte, L. Birkeland, A. Kjekshus, On the Structural and Magnetic Properties of Cr^ FejP, Mn 1 _, Co, P and Fe t _, Co, P, Acta Chemica Scandinavia A, 32 (1978) 731-735.
[61] B.D. Yu, M. Scheffler, Physical origin of exchange diffusion on fcc (100) metal surfaces, Physical Review B, 56 (1997) R15569.

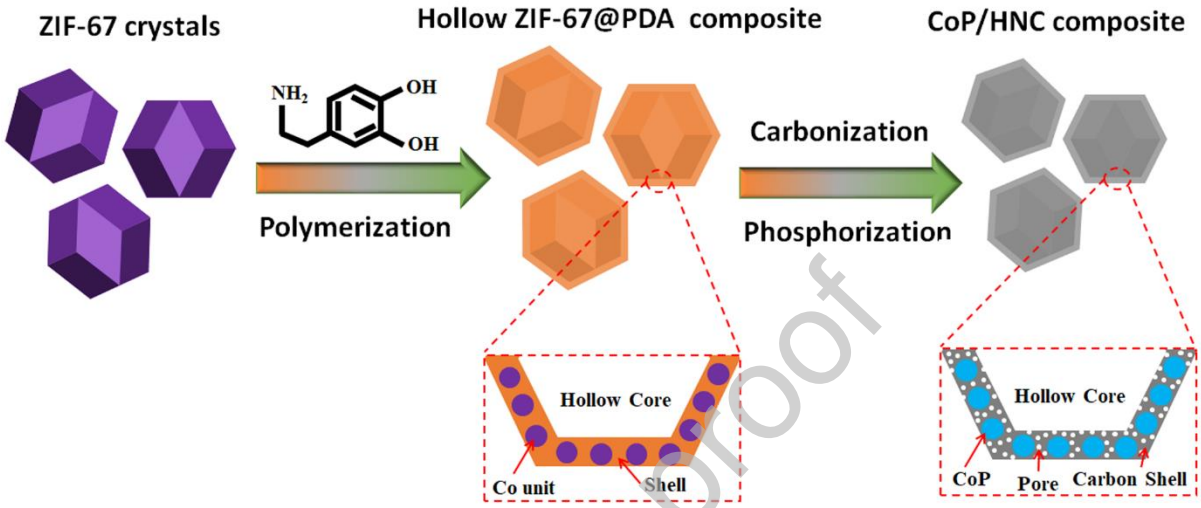

Scheme 1. Schematic illustration of the CoP nanoparticles encapsulated in nitrogen-doped carbon networks (CoP/HNC). Not drawn to real scale.

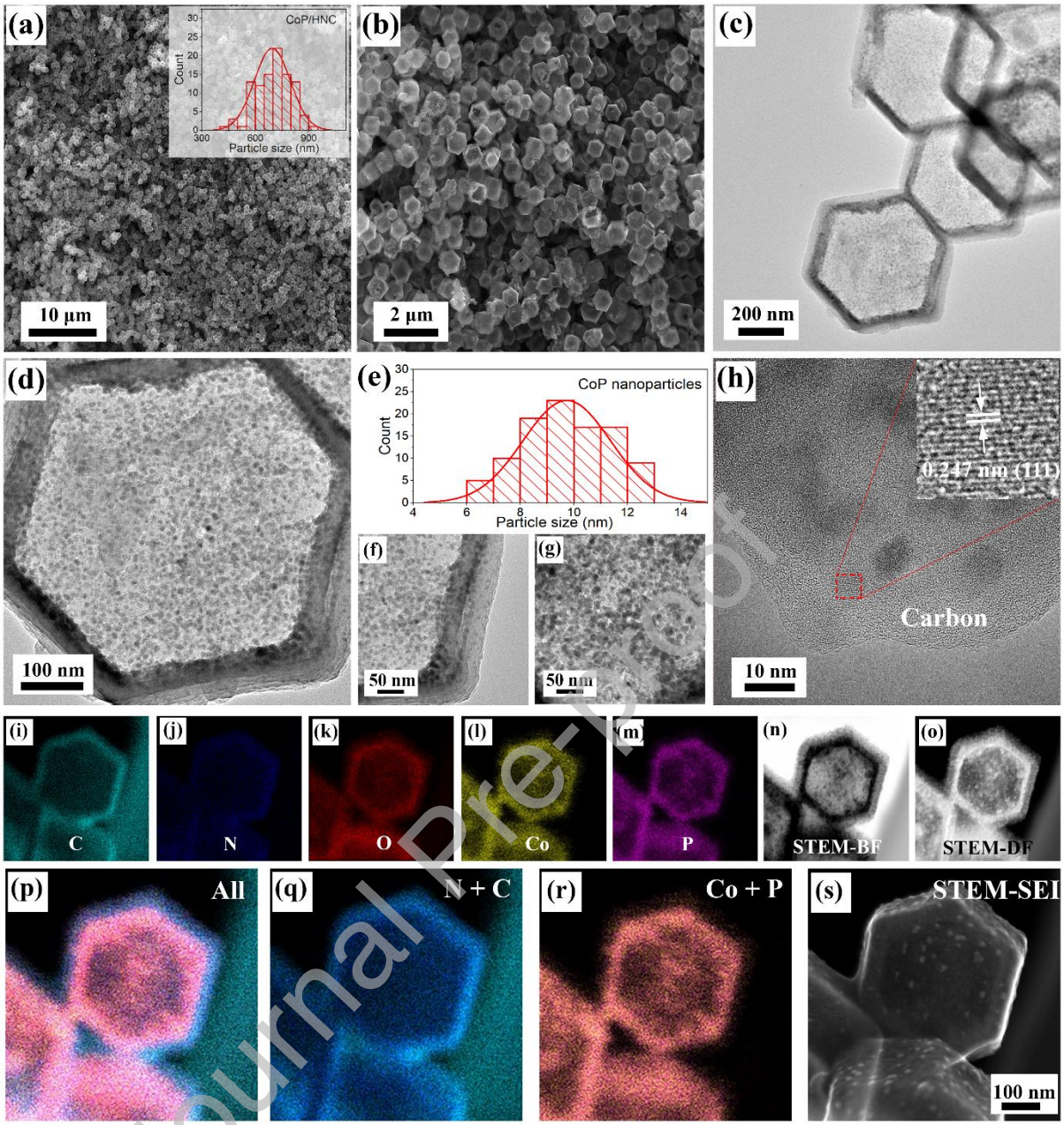

Fig. 1. SEM (a, b) and TEM (c, d) images of CoP/HNC. (e) Particle size distribution of CoP nanoparticles corresponded to (d). (f, g) TEM images of the edge (f) and interior (g) of a single CoP/HNC particle. (h) The high-resolution TEM image of CoP/HNC. (i-m) Individual EDS elemental map; (n) Bright-filed; (o) Dark-field; (p-r) Superimposed EDS elemental mapping of all (p), N + C (q) and Co + P (r); (s) Secondary electron TEM images of the partial CoP/HNC.

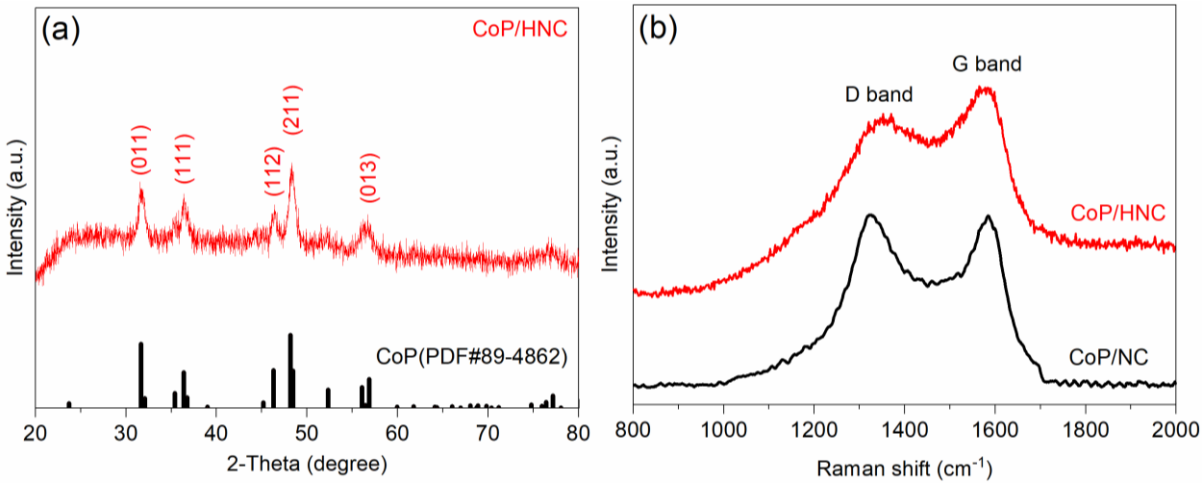

Fig. 2. (a) XRD patterns of the CoP/HNC composite. (b) Raman spectra of the CoP/HNC and Co/NC composite.

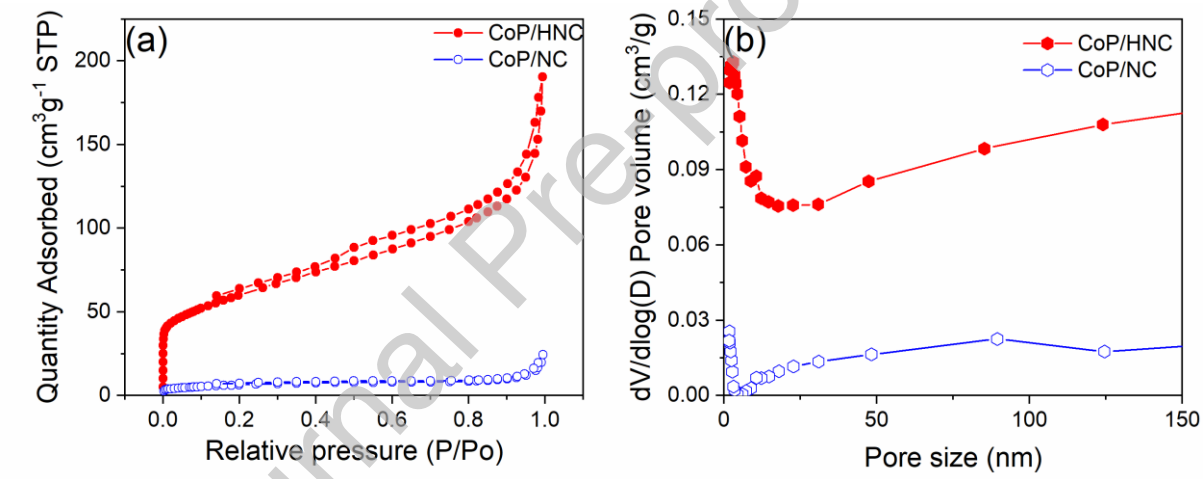

Fig. 3. (a) Typical nitrogen adsorption-desorption isotherms and (b) pore-size distribution of CoP/HNC and CoP/NC composites.

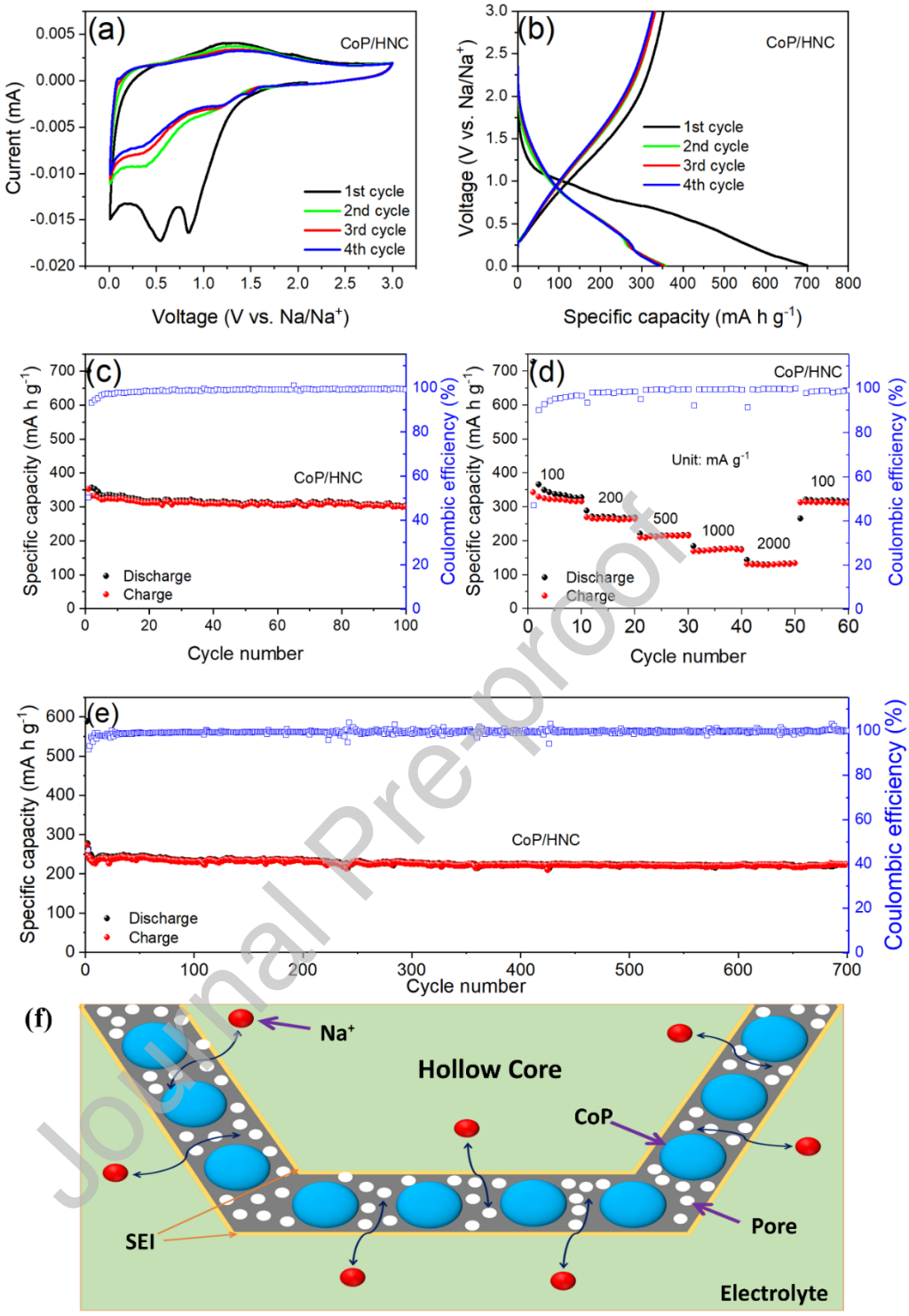

Fig. 4. Electrochemical testing of the CoP/HNC composite: (a) Cyclic voltammograms (CVs) of the first four cycles at a scan rate of 0.1 mV s^{-1}; (b) Galvanostatic discharge/charge profiles of the first four cycles at a current density of 100 mA g^{-1}; (c) Cycling performance at a current density of 100 mA g^{-1}; (d) Rate capabilities at a range of current densities from 100 to 2000 mA g^{-1}; (e) Long-term cycling performance at a current density of 500 mA g^{-1}; (f)

Schematic illustration of the underling mechanism of sodium storage in the CoP/HNC electrode.

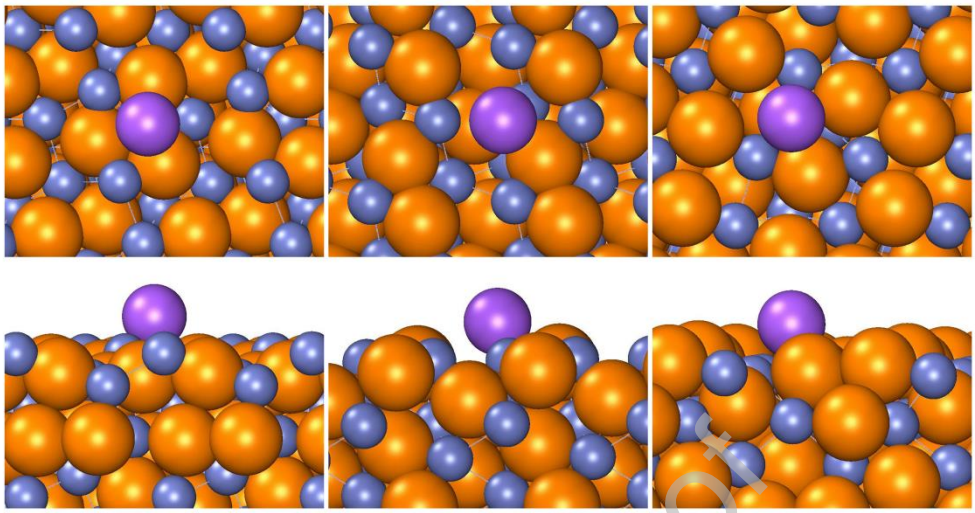

Fig.5. Top and side view of the most stable position of one Na atom adsorbed on a) CoP(111), b) CoP(110), c) CoP(211). The Co, P and Na atoms are colored in cyan, yellow and purple.

Table 1 Na adsorption energy in eV on CoP surfaces for the structures illustrated in Fig. S17.

substrate	CoP(111)	CoP(110)	CoP(211)	graphite
Eads (eV)	-2.09	-2.09	-2.39	-0.57

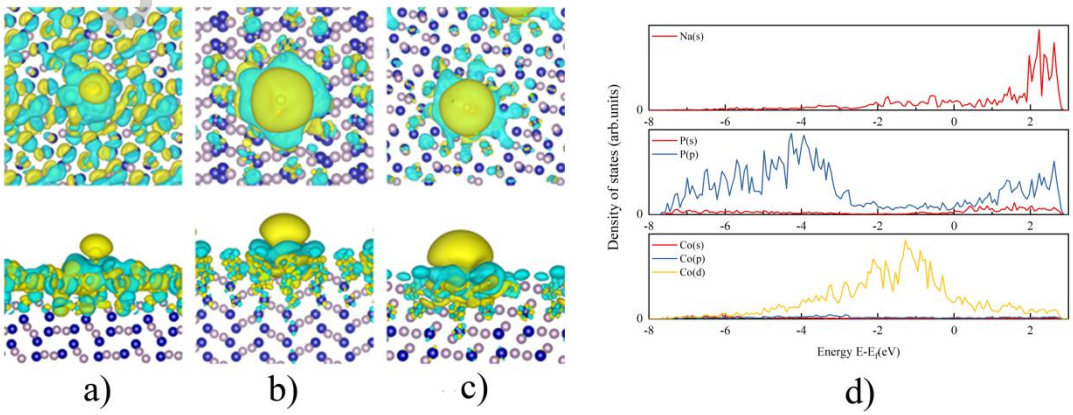

Fig.6. Isosurface plots of charge density differences upon Na adsorption on CoP(111) surface (value 0.004 e/Å3). Charge accumulation, i.e. accumulation of electron density is plotted in light blue, charge depletion in yellow.